

Ocean acoustic wave propagation and ray method correspondence: internal wave fine structure

Katherine C. Hegewisch, Nicholas R. Cerruti and Steven Tomsovic
Department of Physics, Washington State University, Pullman, Washington 99164-2814
(September 14, 2018)

Acoustic wave fields propagating long ranges through the ocean are refracted by the inhomogeneities in the ocean's sound speed profile. Intuitively, for a given acoustic source frequency, the inhomogeneities become ineffective at refracting the field beyond a certain fine scale determined by the acoustic wavelength. On the other hand, ray methods are sensitive to infinitely fine features. Thus, it is possible to complicate arbitrarily the ray dynamics, and yet have the wave field propagate unchanged. This feature raises doubts about the ray/wave correspondence. Given the importance of various analyses relying on ray methods, a proper model should, at a minimum, exclude all of the fine structure that does not significantly alter the propagated wave field when the correspondence to the ray dynamics is integral. We develop a simple, efficient, smoothing technique to be applied to the inhomogeneities - a low pass filtering performed in the spatial domain - and give a characterization of its necessary extent as a function of acoustic source frequency. We indicate how the smoothing improves the ray/wave correspondence, and show that the so-called "ray chaos" problem remains above a very low frequency ($\sim 15 - 25$ Hz).

PACS numbers: 43.30.Cq, 43.30.Ft, 43.20.Dk

I. INTRODUCTION

As acoustic waves propagate long ranges through the deep ocean, they are refracted by inhomogeneities in the ocean's sound speed profile. Roughly speaking, in the earth's mid-latitudes, temperature and pressure effectively combine to form a wave guide in the depth coordinate that vertically confines the propagation¹. In addition to this overall structure, the ocean behaves as a weakly turbulent medium² that multiply scatters the acoustic waves mainly in the forward direction. Whether one is intrinsically interested in waves propagating through weak turbulence or in the state of the ocean through tomography¹, ray methods are relied upon at various stages and levels of complexity in the resulting experimental analyses³⁻⁵. It is therefore critical to understand the applicability and limits of these ray methods.

Ray methods can only capture the physics of refraction and reflection, unless a geometric theory of diffraction is explicitly added^{6,7}. Intuitively, one expects refractive effects to dominate diffraction when

sound speed inhomogeneities are larger than the acoustic wavelength of the source. On the other hand, due to their pointlike nature, rays are sensitive to structures at all scales. Thus, one should be suspicious of (non-diffractive) ray methods for models that have significant fine scale structure that are ineffective in refracting waves, but that fundamentally alter the rays themselves. Hence, certain fine scale structures in the model can be thought of as being physically irrelevant, i.e. having no influence on the wave propagation, and should be eliminated before applying a ray method analysis. The possibility of diffraction is very important, but should be dealt with separately and we do not discuss it further in this article.

Another serious challenge for the applicability of ray methods that has been recognized in the past fifteen years or so, is the existence of ray chaos⁸; see also earlier work in the field of quantum chaos⁹⁻¹². One typical argument goes that chaos introduces caustics, i.e. singularities, in ray methods at an exponentially increasing rate with propagation time (range). Ray methods must therefore breakdown on a logarithmically short propagation scale, which renders them essentially useless. A significant body of work has shown that this need not be the case, and methods can be developed which are accurate to much longer propagation scales^{13,14}. Even so, detailed ray methods tend to become rather burdensome with the exponential proliferation of rays. Thus, resorting to statistical methods based on the chaotic properties of the rays is often attractive.

These two reservations about ray methods, inclusion of physically irrelevant fine structures in the sound speed profile and ray chaos, have often been co-mingled. For example, it is possible to add very fine structure to a sound speed model that has no effect on propagating waves and yet generates chaotic rays as unstable as one wishes. Our point of view is that the two issues should be disentangled, necessarily beginning with the removal of the physically irrelevant fine structures, whose characterization depends on the acoustic wavelength. We will come back to the ray chaos question, but leave a more detailed and complete analysis for follow-up work to this paper.

Our purpose is, thus, to create a practical and easily implemented technique for smoothing inho-

mogeneities in a sound speed model, and to give prescriptions for the extent of smoothing needed as a function of source frequency. Toward these ends, it is not necessary to mimic a realistic ocean accurately with the model, but rather to include certain key features, such as a simple form for the waveguide confinement and the fluctuations due to the weak turbulence. It is more than sufficient to include scattering solely in the vertical spatial plane, to make the parabolic approximation¹⁵ and to neglect larger mesoscale structures. A simple ocean sound speed model uses Munk’s canonical model¹⁶ to account for large scale effects due to temperature, pressure and salinity, and an efficient implementation scheme by Colosi and Brown¹⁷ to generate much smaller inhomogeneities due to the ocean’s internal waves. Using their approach, the inhomogeneities have the statistics of the Garrett-Munk spectrum¹⁸. These features, though leading to a simplified model of the ocean, are more than adequate for investigating the length scale at which fluctuation features become important. Increased realism will be included in a future companion paper¹⁹.

The outline is as follows. In Section II, the ocean sound speed model and the method for acoustic propagation are presented. The following section considers theoretical issues such as the convergence of the propagated wave field by asking the question: “does adding more modes in the internal wave expansion cease altering the propagation beyond some maximum mode number?”. In Section IV, a smoothing of the expression for the internal wave sound speed model is introduced. This smoothing is very similar to the application of a low-pass filter - it removes most of the structures in the sound speed model that are shorter than a certain scale - but it is done directly in the spatial domain so that ray methods can easily be applied. Sensibly, the optimal amount of smoothing necessary is a function of source frequency. We demonstrate the effects of smoothing on both the wave field propagation and on the phase space structures associated with the underlying ensemble of rays. This does not, in general, eliminate the consideration of ray chaos as the Lyapunov exponents are still positive, but it does remove a significant amount of the so-called “micro-folding”²⁰ of the phase space structures. We discuss how this can markedly improve the ray/wave correspondence.

II. THE ACOUSTIC PROPAGATION MODEL

In a medium such as the ocean where density fluctuations are small, the wave equation accurately describes the acoustic waves in which we are interested.

The governing equation is

$$\frac{\partial^2}{\partial t^2} \Phi(\vec{r}, t) = c^2(\vec{r}, t) \nabla^2 \Phi(\vec{r}, t), \quad (1)$$

where $\text{Re}\{\Phi(\vec{r}, t)\}$ is the acoustic pressure and $c(\vec{r}, t)$ is the sound speed at a location \vec{r} and time t . The mean sound speed is roughly 1.5 km/s and if we consider a water parcel, the sound passes through it far faster than any variation in $c(\vec{r}, t)$ due to the internal waves; i.e. the internal waves travel several orders of magnitude more slowly than the acoustic waves. Hence, it is reasonable to ‘freeze’ the state of the ocean and let $c(\vec{r}, t) = c(\vec{r})$.

In anticipation of treating long range propagation, we assume that the scattering in the azimuthal direction is negligible and the important components of the acoustic wave field propagation take place in two spatial dimensions with $\vec{r} = (z, r)$, where z is depth in the ocean and r is range from the source. Consider a constant frequency source, i.e. a pure sinusoidal source of angular frequency $\omega = 2\pi f$ with frequency f , whose amplitude is constant in time. Then, the wave field has a frequency response, $\Phi_\omega(z, r)$, where $\Phi(z, r, t) = \Phi_\omega(z, r) e^{-i\omega t}$. With this assumption, the wave equation reduces to the Helmholtz equation in cylindrical coordinates

$$\nabla^2 \Phi_\omega(z, r) + k^2(z, r) \Phi_\omega(z, r) = 0, \quad (2)$$

where the wave number $k(z, r) = \omega/c(z, r)$.

A. The Parabolic Equation

For long range propagation, waves that propagate too steeply with respect to the horizontal strike the ocean bottom and are strongly attenuated. Since the surviving waves propagate at small angles with respect to the horizontal, a Fresnel approximation¹⁵ is possible which expresses the acoustic frequency response as the product of an outgoing cylindrical wave, $e^{ik_0 r}/\sqrt{r}$ and a slowly varying envelope function, $\Psi_\omega(z, r)$, where the horizontal wavenumber $k_0 \approx \omega/c_0$. Thus,

$$\Phi_\omega(z, r) = \Psi_\omega(z, r) \frac{e^{ik_0(\omega)r}}{\sqrt{r}}. \quad (3)$$

Substituting Eq. (3) into Eq. (2) and dropping two small terms gives the parabolic equation

$$\frac{i}{k_0} \frac{\partial}{\partial r} \Psi_\omega(z, r) = -\frac{1}{2k_0^2} \frac{\partial^2}{\partial z^2} \Psi_\omega(z, r) + V(z, r) \Psi_\omega(z, r). \quad (4)$$

Since the sound speed can be decomposed into the reference sound speed, c_0 , and fluctuations, δc , about the reference: $c(z, r) = c_0 + \delta c(z, r)$ with

$\delta c(z, r) \ll c_0$, the potential is approximated as follows:

$$V(z, r) = \frac{1}{2} \left(1 - \left(\frac{c_0}{c(z, r)} \right)^2 \right) \approx \frac{\delta c(z, r)}{c_0}. \quad (5)$$

In our calculations, we'll use the last form of Eq. (5) for simplicity. Notice that there is a direct analogy between this parabolic equation and the quantum mechanical Schrödinger equation through the substitutions: $t \rightarrow r$, $m \rightarrow 1$, and $\hbar \rightarrow 1/k_0$. We use a symmetric split-operator, fast-Fourier-transform method to propagate the wave field^{21,22}; see Appendix A.

The two terms neglected on the right side of Eq. (4) are

$$\frac{1}{8k_0^2 r^2} \Psi_\omega(z, r) + \frac{1}{2k_0^2} \frac{\partial^2}{\partial r^2} \Psi_\omega(z, r). \quad (6)$$

The first term falls off rapidly with range since $k_0 r \gg 1$. The second term is dropped due to the parabolic approximation which assumes that for a slowly varying envelope function, the curvature is weak. Note that up to this point, we have also dropped other terms from the propagation equation in assuming negligible azimuthal scattering and negligible time dependence of the internal waves. See the discussion in Ref. 23 for more details on all of the terms that have been dropped and an order of magnitude estimate for the size of the various contributions.

B. Ocean Sound Speed Model

A simple model for the speed of sound in the ocean consists of two main components. The first component of the model is an adiabatic, large scale behavior which is responsible for creating the ocean's 'sound channel' - an effective wave guide for acoustic propagation in the deep ocean. This general behavior has a minimum sound speed at the sound channel axis, and varies slowly with latitude and season, with the sound channel axis moving toward the surface for higher latitudes and colder seasons. Mesoscale variability is neglected in this study. The second component of the model is local fluctuations in the sound speed due to the ocean's internal waves. These fluctuations are much smaller in magnitude than the wave guide confining behavior, but describe the range dependence. The model potential $V(z, r)$ takes the form

$$V(z, r) = \frac{\delta c(z, r)}{c_0} = \frac{\delta c_{wg}(z)}{c_0} + \frac{\delta c_{iw}(z, r)}{c_0}, \quad (7)$$

where δc_{wg} represents the change of the sound speed due to the wave guide, which we take to be range independent, and δc_{iw} represents the fluctuations due to internal waves.

1. The Confinement/Wave Guide

In the ocean, the main effects of pressure, temperature, and salinity create a minimum in the sound speed. Since sound bends toward regions of lower velocity, the shape of the sound speed profile refracts propagating waves toward the sound channel axis. This effect is captured in a smooth, average model proposed by Walter Munk¹⁶ and is known as Munk's canonical model

$$\frac{\delta c_{wg}}{c_0} = \frac{B\gamma}{2} \left[e^{-\eta(z)} - 1 + \eta(z) \right], \quad (8)$$

where $\eta(z) = 2[z - z_a]/B$, z_a is the sound channel axis, B is the thermocline depth scale giving the approximate width of the sound channel, and γ is a constant representing the overall strength of the confinement. This model has its minimum speed at $z = z_a$ and captures the right exponential and linear trends near the surface and bottom. The parameters are chosen to be $B = 1.0$ km, $z_a = 1.0$ km, $c_0 = 1.49$ km/s and $\gamma = 0.0113$ km⁻¹, which are roughly consistent with the well known environmental measurements performed in the SLICE89 experiment^{24,25}.

2. Internal Wave Sound Speed Fluctuations

Internal wave fluctuations perturb the sound speed in the ocean through the resultant vertical motions of water parcels. They are responsible for multiple, weak, forward scattering of acoustic waves. A numerical scheme has been introduced by Colosi and Brown¹⁷, which allows efficient computation of a random ensemble of individual realizations of the typical sound speed fluctuations. This scheme conforms to the Garrett-Munk spectral and statistical phenomenological description of the internal waves^{18,26} and has the form

$$\frac{\delta c_{iw}}{c_0} = \sum_{j=1}^{J_{max}} \sum_{k_r} e_{j,k_r} \exp\left(-\frac{3z}{2B}\right) \sin(j\pi\xi(z)), \quad (9)$$

where we took $\xi(z) = e^{-z/B} - e^{-H/B}$ with H the depth of the ocean. The prefactor e_{j,k_r} includes a random phase and magnitude factor for each j and k_r in the sum; see Appendix B for further details and to infer a definition of e_{j,k_r} . Since the frequency of vertical motions lie between the inertial frequency,

due to the earth's rotation, and the buoyancy frequency, due to the local stratification, the sum over the horizontal wave vector k_r has terms representing the superposition of internal waves with wavelengths in the range of 1 – 100 km. A maximum for the j -summation has been chosen as $J_{max} = 180$, which gives structure down to the scale of roughly a meter. The modes, $\sin(j\pi\xi(z))$, are connected to the buoyancy profile which is assumed to have an exponential form. Although the form given in the text above for $\xi(z)$ does not vanish precisely at the surface, it is sufficient for our purposes.

The model should enforce that both the function δc_{iw} and its derivative vanish sufficiently smoothly at the surface. Thus, a surface filter is introduced which consists of multiplying Eq. (9) by a continuous function of depth with the properties that it vanishes above the ocean's surface, is unity below 200 m, and has continuous first and second derivatives. In this way, $\delta c_{iw}/c_0$ and its derivative vanish at the surface and are fully, smoothly restored below 200 m. Since the upper 200 m of the ocean can be quite complex with storms, seasonal fluctuations and latitudinal variability, there is no simple, general sound speed model near the surface; the surface filter is adequate for our purposes. We will propagate waves for which very little energy will enter this region, and thus, little effect of this surface smoothing will be relevant. The specific form we have chosen for the surface filter is

$$g(z; z_{st}, \tau_{st}) = \begin{cases} 0 & \text{for } z' \leq -1/2 \\ h(z') & \text{for } |z'| \leq 1/2 \\ 1 & \text{for } z' \geq 1/2 \end{cases}, \quad (10)$$

where $z' = (z - z_{st})/\tau_{st}$, the width is $\tau_{st} = 200$ m, the center is $z_{st} = \tau_{st}/2 = 100$ m, and the smooth function in between is

$$h(z) = \frac{1}{2} + \frac{9}{16} \sin(\pi z) + \frac{1}{16} \sin(3\pi z). \quad (11)$$

C. Initial Wave Field

The parabolic equation requires an initial wave field $\Psi_\omega(z, r = 0)$ as input, which can then be propagated to the desired range of interest. It is important to understand the connection between the initial wave field and the localized, continuous wave source. Typical sources can be thought of as point sources whose acoustic energy disperses broadly. However, due to the previously mentioned fact that all the steeply propagating waves are strongly attenuated, we can instead propagate only that wave energy moving sufficiently close to the horizontal (within a spread of angles from the sound channel axis) that

would have avoided the ocean's surface and bottom. Restricting the propagation angles limits the size of the vertical wave vector and necessarily creates "uncertainty" in the location of the point source. For our purposes, it is appropriate to choose $\Psi_\omega(z, 0)$ to be a minimum uncertainty wave packet. This implies using a normalized Gaussian wave packet of the form

$$\Psi_\omega(z, 0) = \left(\frac{1}{2\pi\sigma_z^2} \right)^{\frac{1}{4}} \exp \left(-\frac{(z - z_0)^2}{4\sigma_z^2} + ik_{0z}(z - z_0) \right), \quad (12)$$

where z_0 centers the field, σ_z is the standard deviation of the Gaussian intensity and k_{0z} gives the propagating field an initial wavenumber in the z -direction. In all our calculations, we set $k_{0z} = 0$, which maximizes the horizontally propagating energy, and $z_0 = z_a$, which centers the energy on the sound channel axis.

A Fourier transform of Eq. (12) yields a complex Gaussian distribution of initial vertical wave numbers, k_z , centered at k_{0z} with standard deviation in intensity, σ_k . Since σ_z^2 and σ_k^2 are the variances of the intensity and not the amplitude of the wave, their relation is $\sigma_z^2 = 1/4\sigma_k^2$. By a simple geometrical argument, a vertical wavenumber can be related to the horizontal wavenumber by $k_z = k_0 \tan \theta$, where θ is the angle with respect to the sound channel axis. In the next subsection, it is seen that $p = \tan \theta$ is a generalized momentum for a classical ray corresponding to the wave. Classical rays with the maximum angle θ_{max} just barely graze the surface or bottom, and thus, rays are limited in their vertical wave numbers. Yet, for Gaussian wave packets, all wave numbers are in principle present, though most are weighted negligibly by the tails. It is the width, σ_k , which determines if the wave contains wave numbers large enough for a substantial amount of the wave to hit the surface or the ocean floor. One can determine a proper Gaussian width, in order for only the Gaussian tails to pass the surface or bottom, in analogy with the limiting classical rays by letting the maximum classical wavenumber $k_0 \tan \theta_{max}$ correspond to three standard deviations out in the initial Gaussian wavenumber distribution, i.e. set $3\sigma_k = k_0 \tan \theta_{max}$. Then

$$\sigma_z^2 = \frac{9}{4k_0^2 \tan^2 \theta_{max}}. \quad (13)$$

The explicit dependence of σ_z on the angular frequency, ω , of the continuous wave source is realized using the approximate relation $k_0 \approx \omega/c_0$.

The specific choice of θ_{max} depends on the vertical confinement. For the background confinement in Eq. (8), those rays departing the sound channel axis

with an angle of $\theta = \pi/18$ (10°) come within 150 m of the surface, and those with $\theta = \pi/15$ (12°) come within 30 m. The addition of internal waves to the sound speed model causes some rays to have a closer approach to the surface, so we will most often use $\theta_{max} = 10^\circ$ in this paper.

D. The Classical Rays

From the parabolic equation, one can derive a Hamiltonian system of equations for the position, z , and generalized momentum, p , of the collection of rays corresponding to the wave propagation. The Hamiltonian is given by $H = p^2/2 + V(z, r)$ and the potential is $V(z, r) = \delta c(z, r)/c_0$. The equations are

$$\begin{aligned} \frac{dz}{dr} &= \frac{\partial H}{\partial p} = p \\ \frac{dp}{dr} &= -\frac{\partial H}{\partial z} = -\frac{\partial V(z, r)}{\partial z}. \end{aligned} \quad (14)$$

Since $dz/dr \approx \Delta z/\Delta r = \tan \theta$, the generalized momentum is $p = \tan \theta$. The classical action T is calculated by imposing the initial condition $T_0 = 0$ and using the relationship

$$\frac{dT}{dr} = p \frac{dz}{dr} - H. \quad (15)$$

Through the parabolic approximation, the classical action is directly related to the travel time, τ , of the acoustic waves, where $T = c_0 \tau - r$.

The relevant rays to the wave propagation are those appropriate for a Gaussian wave packet^{14,27}, which implies initial conditions in the neighborhood of (z_0, p_0) . Since $k_{0z} = k_0 p_0 = 0$ for the wave packet in Eq. (12), ray calculations are done in a neighborhood of $p_0 = 0$. However, z_0 is taken to be on the sound channel axis, z_a .

The addition of range dependent internal wave effects to the sound speed model causes the classical rays to be chaotic⁸. The stability matrix contains the information about whether the rays are unstable (chaotic) or not²⁸. At a fixed r , one has

$$\begin{pmatrix} \delta p_r \\ \delta z_r \end{pmatrix} = Q_r \begin{pmatrix} \delta p_0 \\ \delta z_0 \end{pmatrix}, \quad (16)$$

where the stability matrix

$$Q_r = \begin{pmatrix} q_{11} & q_{12} \\ q_{21} & q_{22} \end{pmatrix} = \begin{pmatrix} \left. \frac{\partial p_r}{\partial p_0} \right|_{z_0} & \left. \frac{\partial p_r}{\partial z_0} \right|_{p_0} \\ \left. \frac{\partial z_r}{\partial p_0} \right|_{z_0} & \left. \frac{\partial z_r}{\partial z_0} \right|_{p_0} \end{pmatrix}. \quad (17)$$

Elements of this matrix evolve according to

$$\frac{d}{dr} Q_r = K_r Q_r, \quad (18)$$

where Q_r at $r = 0$ is the identity matrix, and

$$K_r = \begin{pmatrix} -\frac{\partial^2 H}{\partial z_r \partial p_r} & -\frac{\partial^2 H}{\partial z_r^2} \\ \frac{\partial^2 H}{\partial p_r^2} & \frac{\partial^2 H}{\partial z_r \partial p_r} \end{pmatrix}. \quad (19)$$

The system of differential equations Eqs. (14), (15) and (18), are solved using a 4th order Runge-Kutta method (where we have taken $\Delta r = 100$ m in all calculations).

The Lyapunov exponent, μ , is a measure of the rate at which the rays are deviating under small perturbations. The relationship between the Lyapunov exponent and the matrix Q_r comes through the trace (sum of the diagonal elements) of Q_r ,

$$\mu \equiv \lim_{r \rightarrow \infty} \frac{1}{r} \ln |Tr(Q_r)|. \quad (20)$$

If $|Tr(Q_r)|$ grows exponentially, the Lyapunov exponent is nonvanishing and positive, and the corresponding trajectory is chaotic.

III. THEORETICAL CONSIDERATIONS

Wave propagation should become increasingly insensitive to smooth perturbations as the scale of the perturbations decreases to the order of the smallest wavelength in the source and beyond. This issue does not arise in the horizontal coordinate of the internal wave model in Eq. (9), since the fluctuation scales are much longer than the horizontal projections of typical source wavelengths. However, this is an issue for the vertical fluctuations since Eq. (9) is a weighted superposition of a large number of vertical internal wave modes and presumably contains more detail than is necessary for accurate wave propagation. There comes a point in the summation beyond which the vertical modes begin to add physically irrelevant features to the sound speed inhomogeneities for a given source frequency. To determine the transition point where this occurs requires an understanding of the minimum wavelength structure in the propagating wave field, and an understanding of the power spectrum of individual vertical internal wave modes. The transition point, though, is not the only issue since higher modes contain a mix of physically relevant and irrelevant structures. These issues as well as their interplay are discussed here.

A. The Vertical Mode Number Transition

Intuitively, the vertical structures in the sound speed model responsible for refracting the wave are those that are larger than the minimum vertical

wavelength, λ_{min} , in the initial wave packet. Expressions for λ_{min} can be obtained by using $\lambda = 2\pi/k$ and the previously noted geometrical relation $k_z = k_0 \tan \theta$,

$$\lambda_{min} = \frac{2\pi}{k_0 \tan \theta_{max}} = \frac{\lambda_0}{\tan \theta_{max}} = \frac{c_0}{f \tan \theta_{max}}. \quad (21)$$

Recall that the ocean waveguide forces θ_{max} to be small so that the minimum vertical wavelength is always enhanced over the source wavelength, λ_0 . For $\theta_{max} = 10^\circ$, this enhancement is roughly a factor of 6. As a practical example, we note that some of the experiments conducted by the Acoustic Engineering Test (AET)^{3,4} use a broadband 75 Hz source. A pure 75 Hz source has a 20 m source wavelength. Thus, if the energy stripping due to the ocean surface and bottom is consistent with $\theta_{max} = 10^\circ$, then the wave propagation would have a minimum vertical wavelength scale of roughly 110 m.

The vertical structures in the sound speed model in Eq. (9) arise through the superposition of vertical modes of the form $e^{-3z/2B} \sin(j\pi(e^{-z/B} - e^{-H/B}))$. Since the argument of the sine is nonlinear, each vertical mode contributes different oscillation lengths at different depths. The monotonicity of the argument illustrates that each mode has a ‘‘chirped’’ structure, i.e. each mode oscillates more and more rapidly as the surface is approached. To make this more precise, an expansion of the argument of the sine reveals that the local oscillation length as a function of depth is

$$\lambda_{iw}(z, j) = \frac{2Be^{z/B}}{j}. \quad (22)$$

Therefore, the j^{th} internal wave mode contributes its shortest length contribution of $2B/j$ near the surface, with longer length scales at increasing depth. Each mode gives contributions to the sound speed fluctuations over a broad range of scales.

Figure 1 illustrates the depth dependence and power spectrum of an internal wave mode. The power spectrum has a fairly sharp high frequency (short length scale) cutoff from the structures added near the ocean surface and a slowly decaying tail for the lower frequencies (longer length scales). The broad tail for an individual mode indicates that many different modes contribute to a particular size feature in the internal wave model.

The transition vertical mode number J_{trans} can be identified as that point where the vertical modes begin to introduce structure smaller than λ_{min} . Thus, setting Eqs. (21) and (22) equal to each other and solving for j gives

$$J_{trans} = \frac{2B \tan \theta_{max}}{\lambda_0} = \frac{2Bf \tan \theta_{max}}{c_0}. \quad (23)$$

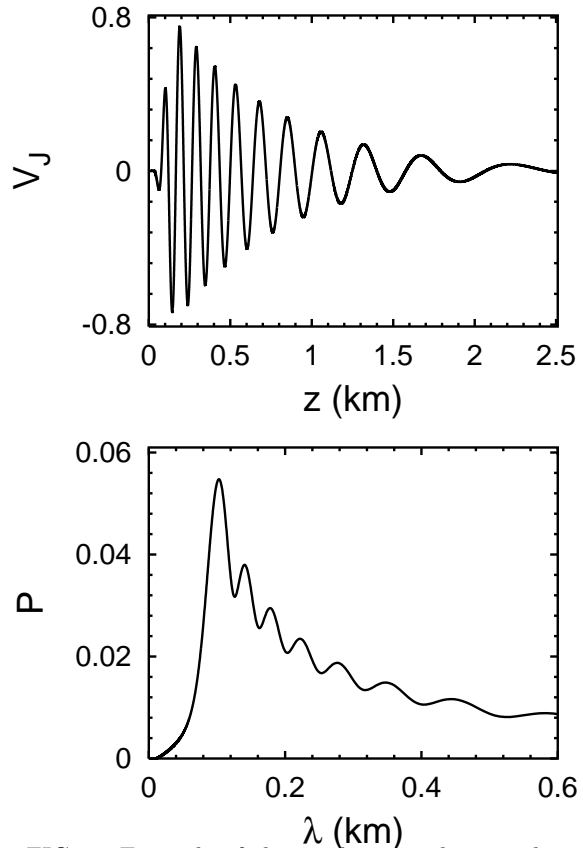


FIG. 1. Example of the single vertical internal wave mode for $j = 25$. The upper plot illustrates its depth dependence, $V_j = g(z; z_{st}, \tau_{st}) e^{-3z/2B} \sin(j\pi(e^{-z/B} - e^{-H/B}))$, where g is the surface filter defined in Eq. (10) and the lower plot is the power spectrum, P , of V_j .

The calculation of J_{trans} does not reflect that each vertical mode is weighted in Eq. (9) by the coefficients e_{j,k_r} , which we numerically found to have root mean square decay $\sqrt{\sum_{k_r} |e_{j,k_r}|^2} \sim j^{-1.1}$ for large j . Thus, the higher vertical modes have a slowly decreasing weighting. The acid test of the effects of both the diminishing amplitudes and the detectability of features by the wave is to look at the sensitivity of the wave field to variations in the value for the j -summation cutoff in Eq. (9).

B. Wave Field Convergence

We can investigate the convergence of the wave field propagation by using different values for the

j -summation cutoff in Eq. (9) to generate various sound speed media. The value of the cutoff leading to a converged wave field, denoted by J_ω , is the minimum number such that by including higher modes there is relatively little change in the wave propagation. We do not have a simple intuitive argument that gives an expression for J_ω , but instead rely on numerical simulations to determine reasonable values.

In order to discuss quantitatively what is meant by ‘little change to the wave propagation’, it is necessary to have a measure of the similarity of two wave fields. An ideal measure is the absolute value squared of the overlap (inner product). For two sound speed potentials that differ by ΔV , the quantity $C_{\Delta V}$ is defined as

$$C_{\Delta V}(r) = \left| \int dz \Psi_\omega^{*\Delta V}(z, r) \Psi_\omega(z, r) \right|^2, \quad (24)$$

where $\Psi_\omega(z, r)$ is understood to be the wave field propagated to range r with the full potential and $\Psi_\omega^{*\Delta V}(z, r)$ is the same initial state propagated using the potential which differs from the full potential by ΔV . It is convenient to normalize the propagating wave fields to unity since this is preserved under the unitary propagation of the parabolic equation. With this choice, the measure gives unity only if the two wave fields are identical. The greater the reduction from unity, the greater the differences between the two propagations, i.e. the lower the faithfulness or fidelity of the propagations.

The full wave propagation is compared to wave propagation for various values of mode number cutoff $J \leq J_{max}$. Thus, ΔV is the internal wave sum for j in the interval $[J + 1, J_{max}]$. Since deviations of $C_{\Delta V}(r)$ from unity indicate that features in the modes $[J + 1, J_{max}]$ were detectable by the wave propagation, the value of J where $C_{\Delta V}(r)$ breaks appreciably from unity determines J_ω .

Sound waves with source frequencies of 25, 75, 150, and 250 Hz were propagated to $r = 1000$ km; see Appendix A for details regarding the propagation. Figure 2 demonstrates the dependence of $C_{\Delta V}(r)$ on J . To interpret this figure, consider the curve for 75 Hz. Above $J = 50$, $C_{\Delta V}(r) \geq .99$ and remains near unity. Thus, we can say that here $J_\omega \approx 50$. Using higher internal wave modes adds no more realism, and only slows down the calculations. A similar argument for the other frequencies gives the values of J_ω listed in Table I. Note that J_ω increases just a little more slowly than linear in source frequency due, in part, to the decreasing weightings.

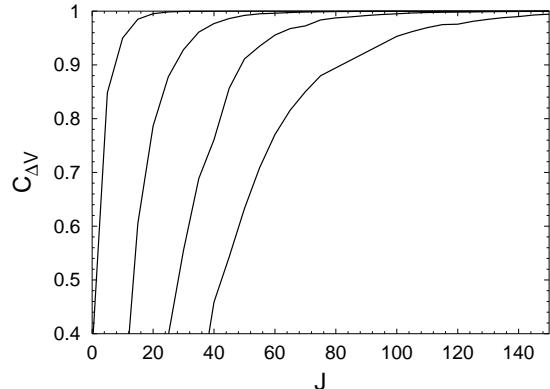


FIG. 2. $C_{\Delta V}(r)$ as a function of J for the source frequencies of 25, 75, 150 and 250 Hz (corresponding to the curves from left to right, respectively) at a range of 1000 km.

TABLE I. Comparison of key parameters for a few viable long range propagation frequencies. Both J_ω and λ_s^{opt} (see the next section) were determined using a conservative 0.99 criterion for the value of the $C_{\Delta V}$ at 1000 km in Figs. 2 and 6. Other choices for the criterion, propagation range, etc... could lead to somewhat greater differences; however the dependences are rather weak. For each calculation, $\theta_{max} = 10^\circ$. Note the minimum wavelength feature, λ_{min} , in the initial wave packet is extremely close to λ_s^{opt} .

Frequency (Hz)	J_{trans}	J_ω	λ_0 (km)	λ_{min} (km)	λ_s^{opt} (km)
25	6	20	0.060	0.340	0.308
75	18	50	0.020	0.113	0.106
150	36	90	0.010	0.056	0.060
250	60	145	0.006	0.034	0.034

Since $C_{\Delta V}$ is inherently range dependent, determining J_ω from a plot of $C_{\Delta V}$ for a single range is potentially inappropriate for longer ranges. Yet, Figure 3 illustrates that the range dependence of $C_{\Delta V}$ is fairly weak for a frequency of 75 Hz. Increasing the range from 1000 km to 4000 km for $J_\omega = 50$ decreases $C_{\Delta V}$ very little from 0.99 to 0.96. Thus, $J_\omega = 50$ is a conservative choice even for ranges up to 4000 km.

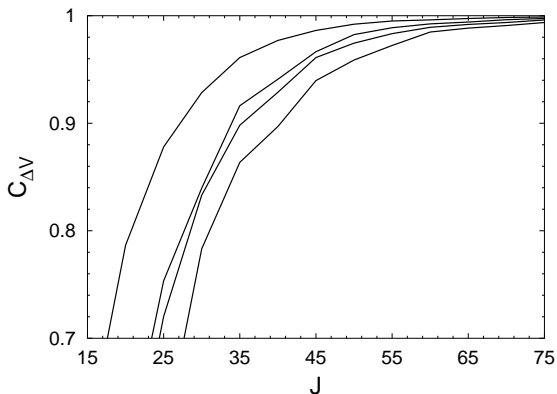


FIG. 3. $C_{\Delta V}(r)$ as a function of J for the ranges of 1000, 2000, 3000 and 4000 km (corresponding to the curves from left to right, respectively) for a frequency of 75 Hz.

For reasonable source frequencies, it is clear that even an optimal choice for J_ω will leave a significant amount of oscillations in the model on a scale much smaller than λ_{min} (since $J_\omega \gg J_{trans}$). Presumably, these oscillations are physically irrelevant for the wave propagation, but it is worthwhile studying more precisely where the cutoff lies within the context of long range propagation.

IV. FILTERING THE PHYSICALLY IRRELEVANT FEATURES

Since we have taken a smooth background sound speed model, the physically irrelevant features of the sound speed model can be removed by filtering the high frequency components from the internal wave sound speed model, $\delta c_{iw}(z, r)$. The ideal approach would be through the application of a low pass filter: Fourier transform $\delta c_{iw}(z, r)$ for a fixed range to a frequency domain, apply a filter that removes the high frequencies and Fourier transform back to give the physically relevant portion of $\delta c_{iw}(z, r)$. There are several drawbacks with respect to proceeding this way. The Fourier transforming back and forth is computationally expensive, creates a problematic

ocean surface, and severely complicates the ray correspondence; the same would be true using a convolution technique. Instead, we develop a smoothing that can be directly applied to each vertical mode in the spatial z domain and serves as a very good approximation to a low-pass filtering in the frequency domain. It takes advantage of the monotonicity of the chirped structure of the individual internal wave modes. The spatial filtering method simplifies the ray equations enormously and allows first and second derivatives to be evaluated exactly, as opposed to numerically, which is an unstable operation.

A. The Smoothing

Due to the precise oscillatory nature of each vertical mode, a good approximation to a low-pass filter can be accomplished by removing the upper portion of the vertical mode that contains oscillations that are smaller than the smoothing parameter, λ_s . This involves multiplying each vertical mode by the function $g(z; z_{sm}, \tau_{sm})$ defined in Eq. (10). This filter is centered at the depth such that the local length scale is λ_s , which by inversion of Eq. (22), gives the mode-dependent depth $z_{sm} = B \ln(j\lambda_s/2B)$. Note that j must exceed $2B/\lambda_s$ in order for the filter to be below the ocean surface, which is where it begins to have an effect. This is consistent with the shortest length contribution of each mode being $2B/j$ at the surface. The width of the filter is carefully chosen to be $\tau_{sm} = 2.0\lambda_s$ so that it does not cut off too sharply thereby introducing high frequency components into the model. If the width were chosen much greater, amplitudes of physically relevant length scales would be reduced.

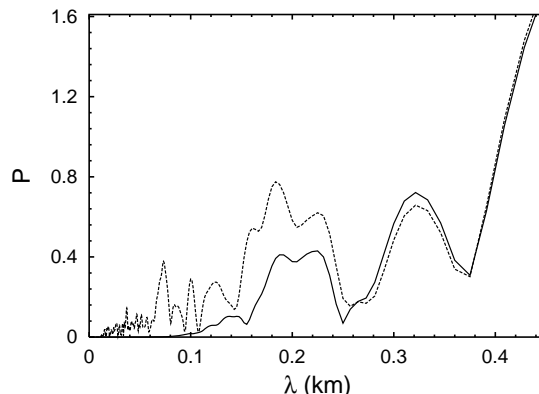


FIG. 4. Effects of the amount of smoothing on the power spectrum, P , of $\delta c_{iw}/c_0$. The dashed line is the power spectrum of the unsmoothed full potential and the solid line is the power spectrum of the smoothed full potential for $\lambda_s = 0.20$ km.

Figure 4 shows the power spectrum of the sound speed model with and without smoothing; it is illustrated with a value, $\lambda_s = 0.2$ km. The power spectrum remains relatively unchanged for length scales greater than 0.2 km, but the length scales below 0.2 km are significantly dampened out of the model. This is evidence that a smoothing parameter of $\lambda_s = 0.2$ km is doing exactly what it was designed to do: it is filtering out features on scales below 0.2 km, but leaving features above 0.2 km in the model. Figure 5 shows the smoothed sound speed potential and the portion of the potential, ΔV , filtered by the smoothing. It is clear from these figures that the oscillations in the unsmoothed potential which have a length scale of less than 0.2 km have been removed, while larger oscillations have been preserved.

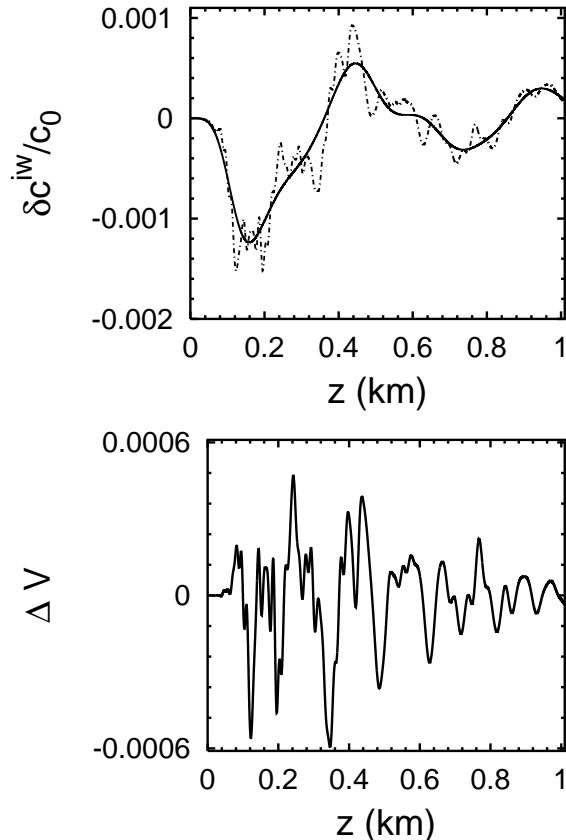


FIG. 5. Effects of the amount of smoothing on the full potential, $\delta c^{iw}/c_0$. In the upper panel, the dashed line is the unsmoothed potential and the solid line is the smoothed potential for $\lambda_s = 0.20$ km. In the lower panel, the difference, ΔV , between the smoothed and unsmoothed potential is displayed.

B. Estimating the Optimal Smoothing Parameter

The optimal smoothing parameter, λ_s^{opt} , would be such that only those features in the model that are not detectable by the wave would be removed. Intuitively, λ_s^{opt} would be very close to λ_{min} of Eq. (21). In order to test this intuition, we again use $C_{\Delta V}(r)$ defined in Eq. (24), where here ΔV is the high frequency portion of the internal wave sum, which the smoothing removes, and the other potential is the full unsmoothed sound speed model. λ_s^{opt} is determined to be the maximum value of λ_s up to which $C_{\Delta V}$ remains nearly unity but deviates significantly beyond.

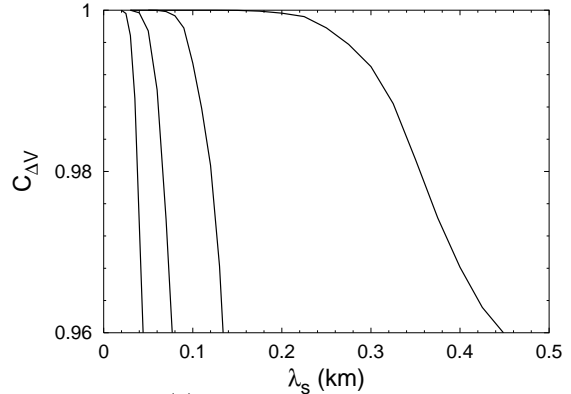


FIG. 6. $C_{\Delta V}(r)$ as a function of λ_s for source frequencies of 25, 75, 150 and 250 Hz (corresponding to the curves from right to left respectively) at a range of 1000 km.

As in the previous section, source frequencies of 25, 75, 150, and 250 Hz were propagated to $r = 1000$ km with J chosen for each frequency to be that value of J_ω in Table I. Figure 6 demonstrates the dependence of $C_{\Delta V}(r)$ on different values of λ_s and its interpretation is similar to that done for Fig. 2. Consider the curve for 75 Hz. Above $\lambda_s \approx 0.1$ km, $C_{\Delta V}$ breaks significantly from unity giving the optimal smoothing of the sound speed model for a 75 Hz source to be $\lambda_s^{opt} \approx 0.1$ km. Smoothing less than this allows high frequency features to remain in the model which have no effect on the wave propagation. Table I summarizes the results which all agree closely with the intuitive idea that $\lambda_s^{opt} \approx \lambda_{min} = \lambda_0 / \tan \theta_{max}$.

For a fixed λ_s , the higher source frequencies lead to a reduced value of $C_{\Delta V}$. This indicates that the high frequency components of ΔV are more detectable by a high frequency source than by a low frequency source. This fully supports the age-old intuitive concept that high frequency waves can detect

smaller features than low frequency waves, and that the appropriate detection scale is a wavelength. A long range propagation experiment utilizing a source frequency f only detects that portion of the internal wave power spectrum with features longer than the length scale $\lambda_{min} = c_0/f \tan \theta_{max}$.

C. Effects of Smoothing on Phase Space Structures

Classical ray methods can be used to reconstruct propagating wave fields in detail through the use of semiclassical Green functions²⁹. The semiclassical approximation to the wave field is

$$\Psi_{sc}(z, r; k_0) = \sum_j A_j(z, r) \exp[ik_0 T_j(z, r) - i\pi\nu_j/2], \quad (25)$$

where the sum is over all ray paths labeled by j that begin at the source and end at a depth z for a given range r . The phase contribution of a path is related to its classical action, T_j , the source wavenumber, k_0 , and the number of caustics, ν_j . The amplitude contribution of a path, A_j , is related to its stability matrix elements; see Ref. 30 for a readable account. This discrete set of paths becomes continuous if we consider all z . Thus, there is a continuous set of rays that underlies the full construction of $\Psi_{sc}(z, r; k_0)$ at a given range. A powerful analysis of the properties of this set comes by considering the rays in the phase space formed by all allowable points given by position and conjugate momentum. Viewed in phase space, the continuous set of rays underlying the wave field propagation (in the single degree of freedom problem being discussed here) forms a continuous, self-avoiding line which is called a manifold. As the range increases, the manifold evolves into a rather wild-looking “spaghetti”. The more chaotic the system, the wilder the appearance of the manifold.

The construction of Eq. (25) relies on the use of stationary phase approximations, which can only be applied reliably when the phase between successive stationary phase points is greater than order unity. Care must be taken in defining the meaning of successive in this context. Thus, Eq. (25) breaks down when $[T_j(z, r) - T_{j'}(z, r)] < k_0^{-1} = \lambda_0/2\pi$ where j and j' are the classical paths/rays corresponding to successive stationary phase points. We term this the ‘area- $(\lambda_0/2\pi)$ rule’ (the translation to this problem of the area- \hbar rule of Refs. 9 and 10). See Refs. 13 and 14 for a detailed presentation of the breakdown of the stationary phase approximation in quantum chaotic systems.

The breakdown of stationary phase is intimately related to how the manifold winds and folds its way through phase space. The difference in the classical action for two rays is related to the areas in phase space between the folds of the evolving manifold and the vertical line of the final depth, z , whose intersections with the manifold specify the rays. If these areas become smaller than $\lambda_0/2\pi$, then stationary phase breaks down for that pair of rays and we say that the two stationary phase points are coalescing. By drawing the manifold and filling in areas of $\lambda_0/2\pi$ in the folds, one can immediately see where problems, such as caustics which produce infinite amplitudes, will be occurring in the semiclassical construction. In the simplest case of two coalescing points, an Airy function uniformization is possible. However, if so many coalescing pairs occur that they cannot be isolated from each other, uniformization effectively is no longer possible, and the semiclassical approximation has broken down.

In the work of Simmen, Flatté, and Wang²⁰, they show how the fine features in the internal wave field lead to a phenomenon they termed “micro-folding” in which tiny folds are densely found along the manifold. Clearly, for typical source frequencies in long range propagation, the neighborhoods of the micro-folds violating the area- $(\lambda_0/2\pi)$ rule overlap everywhere with each other. Thus, one anticipates a dense set of singularities in the semiclassical approximation rendering the approach useless.

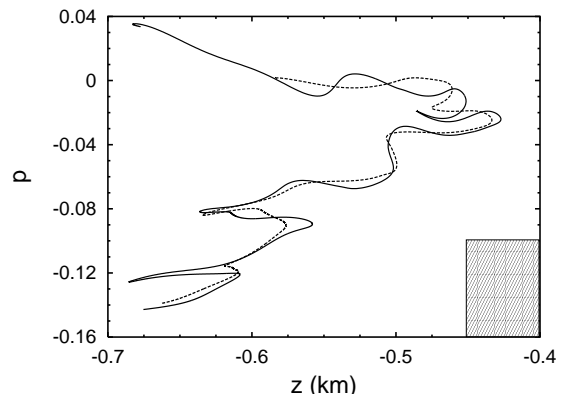


FIG. 7. Smoothed phase space manifold. The solid line is the phase space plot for a dense set of trajectories with launch angle $\theta \in [4^\circ, 8^\circ]$ propagated for 50 km in the unsmoothed ocean model. The dashed line is for the same set of trajectories, but for a smoothing parameter of $\lambda_s = 0.10$ km. All the trajectories started on the sound channel axis. The hatched rectangle is a reference area for physically irrelevant microfolds and has an area $\lambda_0/2\pi$, which corresponds to a 75 Hz source.

Herein lies the advantage of smoothing the ocean

sound speed model of physically irrelevant features before making the ray correspondence. Presumably, the bulk of the micro-folding is related to fine features which are ignored by the wave propagation. The smoothed system contains only that structure necessary to describe the wave propagation so it should have fewer micro-folds. Figure 7 illustrates the effects of smoothing on a set of trajectories. One can see that the smoothed manifold tracks the unsmoothed manifold along its length very well. A more detailed example of micro-folding is illustrated in Fig. 8 for a range of 100 km. Notice how the smoothed manifold completely eliminates this particular micro-folded structure for a smoothing parameter of $\lambda_s = 0.1$ km (appropriate for 75 Hz). Eleven, non-isolated pairs of coalescing stationary phase points were eliminated by the smoothing. Only a well behaved piece of the manifold with no coalescing pairs remains. Thus, there are fewer locations leading to singularities and breakdown in the semiclassical construction for the smoothed system, yet it is describing the same propagated wave. We leave the full semiclassical reconstruction for future work.

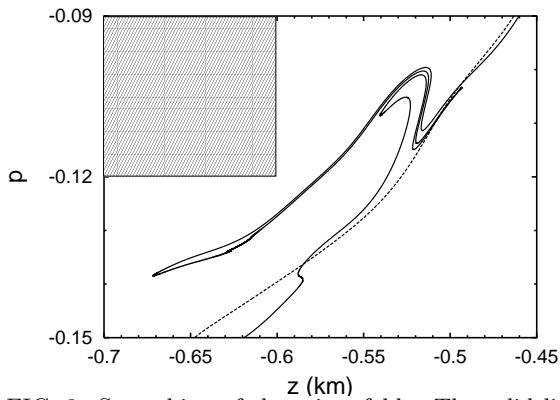


FIG. 8. Smoothing of the micro-folds. The solid line is the phase space plot for a dense set of trajectories with launch angle $\theta \in [7^\circ, 8^\circ]$ propagated for 100 km in the unsmoothed ocean model. The dashed line is for the same set of trajectories, but for a smoothing parameter of $\lambda_s = 0.10$ km. All the trajectories started on the sound channel axis. The hatched rectangle is a reference area for physically irrelevant microfolds and has an area $\lambda_0/2\pi$, corresponding to a 75 Hz source.

D. Effects of Smoothing on Lyapunov Exponent

The following question naturally poses itself from the results of the previous section, “if smoothing the inhomogeneities reduces the number of folds, perhaps it is eliminating the ray chaos that was dis-

covered in Ref. 8?” This turns out not to be the case. The Lyapunov exponents for smoothed systems do not vanish. The Lyapunov exponent, μ , as defined in Eq. (20), requires the infinite range limit, which due to the maximum range of the ocean, is not very sensible. Instead, it is much more relevant to work with finite-range Lyapunov exponents^{31,32}. The stability matrix, Q_r , as defined in Eq. (17), is calculated for a classical ray starting on the sound channel axis with an initial angle θ and propagated for a range r . If $|Tr Q_r|$ is growing exponentially with range, then the ray is unstable or chaotic and the following relationship can be inverted to obtain the finite-range Lyapunov exponent

$$|Tr Q_r| = e^{\mu r} + e^{-\mu r}. \quad (26)$$

Excluding a few highly abstract systems, this μ fluctuates as a function of range and from one ray to the next. In fact, for typical chaotic systems and the internal wave problem here, $|Tr Q_r|$ is close to being lognormally distributed, or from a different point of view, the finite-range Lyapunov exponents give something close to a Gaussian density^{31,32}. The finite-range Lyapunov exponents are launch angle dependent³³. Figure 9 shows histograms of the finite-range Lyapunov exponents for a range of 1000 km for a range of ray angles.

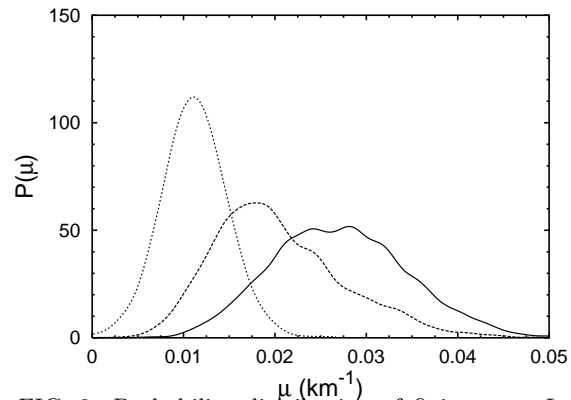


FIG. 9. Probability distribution of finite-range Lyapunov exponents. The range of propagation is 1000 km and each probability distribution consists of 4,000 trajectories within a uniform distribution of launch angles. For the solid line, $|\theta| \in [0^\circ, 2^\circ]$, for the dashed line, $|\theta| \in [4^\circ, 6^\circ]$, and for the dotted line, $|\theta| \in [8^\circ, 10^\circ]$. Each probability distribution was obtained by averaging over a Gaussian window of the corresponding histogram. The smoothing parameter is $\lambda_s = 0.10$ km and all the trajectories started on the sound channel axis.

It turns out that the mean of the finite-range Lyapunov exponents is the usual infinite-limit Lyapunov exponent (as long as one has propagated beyond a

transient range of a few Lyapunov lengths). Letting the brackets $\langle \rangle$ denote averaging over many rays,

$$\mu_0 = \frac{1}{r} \langle \ln |Tr Q_r| \rangle . \quad (27)$$

If one averages before taking the natural logarithm, one gets a second stability exponent which is not the Lyapunov exponent, but rather a related one:

$$\bar{\mu} = \frac{1}{2r} \ln(\langle |Tr Q_r|^2 \rangle) . \quad (28)$$

The relationship between μ_0 and $\bar{\mu}$ for a Gaussian density is through the variance of the distribution of the finite-range Lyapunov exponents

$$\sigma_\mu^2 = \frac{\bar{\mu} - \mu_0}{r} . \quad (29)$$

These two stability exponents fix the Gaussian density completely. Figure 10 illustrates the dependence of μ_0 , $\bar{\mu}$ and the distribution on the smoothing parameter λ_s .

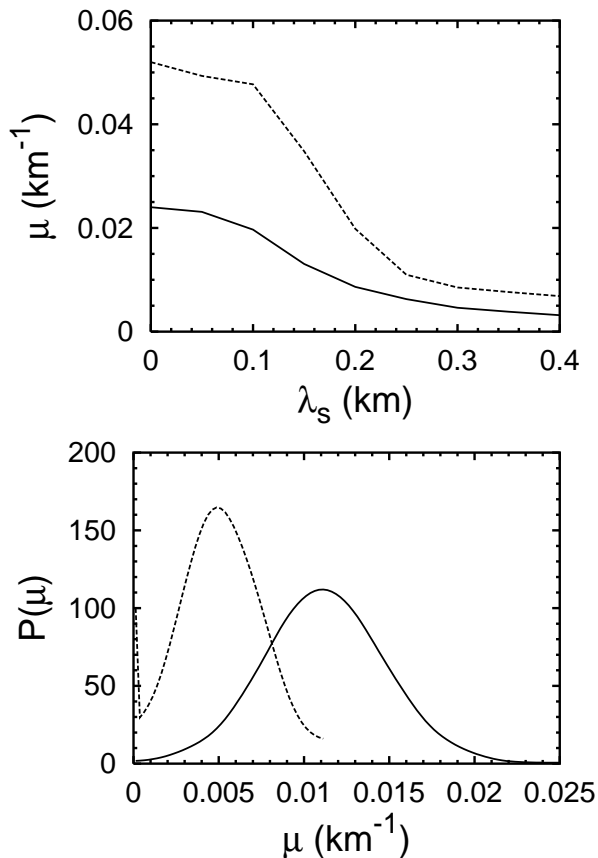


FIG. 10. Average Lyapunov exponents, μ_0 and $\bar{\mu}$, and probability distribution as a function of the smoothing parameter, λ_s . Both plots are for a range of propagation of 1000 km. The upper plot is an average of 2,000 trajectories within a uniform distribution of launch angle $\theta \in [-10^\circ, 10^\circ]$. The solid line is μ_0 and the dashed line is $\bar{\mu}$. The lower plot is the same as the previous plot except that $|\theta| \in [8^\circ, 10^\circ]$ in both curves and the smoothing parameter is varied. The solid line is for a smoothing parameter of $\lambda_s = 0.10$ km and the dashed line is for a smoothing parameter of $\lambda_s = 0.30$ km. A narrow peak near the origin exists in the dashed curve, which indicates a non-negligible fraction of stable trajectories.

Although, there is still ray chaos, the Lyapunov exponent is monotonically decreasing with increased smoothing, but unless a smoothing greater than 0.10 km is applied, μ_0 does not decrease appreciably. At some point, beyond a smoothing somewhere in the neighborhood of 0.3 – 0.5 km, a large fraction of the rays behave stably. Note in Fig. 10 that for $\lambda_s = 0.30$ km, a significant fraction of the rays have become stable, i.e., they have a Lyapunov exponent equal to zero. Using the relation between frequency and optimal smoothing, for source frequencies in the neighborhood of 15 – 25 Hz, there is a transition below which the ray chaos problem due to the internal wave inhomogeneities effectively disappears and above which it remains important over ocean basin scale propagation ranges. Though the background profile used for this study is somewhat simplistic, surprisingly these results seem to be consistent with some very low frequency experiments. In particular, data from the Alternate Source Test (AST) clearly shows that 28 Hz receptions have a more stable arrival pattern than the 84 Hz receptions for transmission over a 5000 km range³⁴.

V. DISCUSSION

In probing the state of the ocean, it is important to understand what information is carried in the wave propagation for a given source frequency. Intuitively, fluctuations in the ocean sound speed on scales shorter than an acoustic wavelength should be ineffective sources of refraction for a sound wave in the ocean. Though, parabolic equation simulations are unaffected by the inclusion of physically irrelevant fine scale fluctuations in the sound speed model (except for the resulting slower computation time), this inclusion worsens the correspondence of ray methods to the wave propagation. On the other hand, ray methods are sensitive to infinitely fine scale structures. Those fine structures that are not

detectable by the wave propagation lead to physically irrelevant micro-folds in the phase space manifolds for the rays. These folds lead to unwanted singularities and the breakdown of semiclassical approximations. Smoothing of the internal wave sound speed model allows a significant reduction in the extent of micro-folding and this must lead to a better ray/wave correspondence.

In our study, we noted that the chirped structure of each of the internal wave modes gives contributions to the sound speed fluctuations over a broad range of scales. Thus, limiting the number of vertical modes used in an internal wave sound speed model does not fully resolve the issue of physically irrelevant fine structure. For the specific construction of Colosi and Brown, our calculations gave frequency dependent values for the number of vertical modes J_ω necessary in the model. For frequencies of $\{25, 75, 150, 250\}$ Hz, we found that the wave field propagation is essentially converged for $J_\omega = \{20, 50, 90, 145\}$, respectively. However, for the same set of frequencies, modes greater than the transition modes $J_{trans} = \{6, 18, 36, 60\}$, respectively, add structures on a finer scale than λ_{min} . Hence, each mode contains a large spread of frequency contributions so that a low-pass filtering of each vertical mode is needed.

In order to remove physically irrelevant structures, we constructed an approximation in the position domain to a low-pass filter by taking advantage of the monotonicity of the chirped structure of each mode. The accuracy of this approximation (though not shown in this paper) was very good for individual modes. The spatial filtering method that we developed gives three main advantages: reducing required computations, better behavior in the neighborhood of the ocean's surface, and simplicity with respect to making the ray correspondence. With this study, it was found that the vertical scale of interest for the vertical fluctuations is not the source wavelength, $\lambda_0 = c_0/f$, but rather the minimum vertical wavelength present in the wave field, which contains the additional projection factor $(\tan \theta_{max})^{-1}$; see Eq. (21). θ_{max} is the largest angle with respect to the horizontal that waves can propagate without being stripped out by bottom interactions and is typically in the neighborhood of $10^\circ - 12^\circ$ in the ocean's mid-latitudes. For these values of θ_{max} the minimum vertical wavelength is roughly 5 – 6 times λ_0 ; i.e. relevant vertical structures are much larger than that implied by λ_0 .

Additionally, from the results in Table I, J_ω scales more slowly with increasing frequency than J_{trans} . This appears to be due to the decreasing weighting of the terms in Eq. (9), which directly influences the convergence of the wave field propagation and the

value of J_ω . If this trend were to continue, then at a sufficiently high frequency, J_{trans} would overtake J_ω in value. Beyond this frequency, low-pass filtering would no longer serve any purpose; one could simply choose an appropriate J_ω . We do not attempt to extrapolate to that point here using our calculations and model, but note that wherever it is, the frequency would be so high that very long-range acoustic propagation would not be possible due to dissipation. However, it may be useful in the context of short range acoustic experiments using much higher frequencies to establish a cross-over frequency with a more realistic model.

We found that smoothing the internal wave sound speed fluctuations does not, in general, eliminate the problems associated with ray chaos. The Lyapunov exponents are positive and significant unless the smoothing scale exceeds 300 - 500 m. Thus, in this simplified model, ray chaos continues to be an important issue for source frequencies above the 15 - 25 Hz range.

A number of difficulties arise in the study of chaotic systems. For example, the exponential proliferation of rays, makes it impractical to carry out ray methods. A common technique to overcome these difficulties is to apply various statistical methods whose justification derives from the chaos itself. However, even if you wish to apply these statistical methods, the validity of semiclassics is still an issue.

Though it is known in the literature that the background sound speed profile can dramatically affect the complexity of the ray dynamics, it is still a question for investigation as to how significant these effects are on the wave propagation. Here we use Munk's canonical model as a simple, smooth background profile, which is sufficient for a study of the removal of physically irrelevant structures. However, before inferring detailed properties of long range experimental data, it would be good to employ a more realistic background sound speed wave guide. In fact, this would require a method for removing fine scale structures from the background in addition to the internal wave model and would not likely be subject to as simple a spatial filtering scheme as we used for the internal waves. We will address these issue in a forthcoming paper.

A number of interesting questions remain or emerge from our results. Our computations did not use pulsed sources, which can be expressed as an integral over a range of frequencies. It would seem reasonable to assume that the dynamics should be smoothed less for higher frequencies than for appreciably lower frequencies. How much attention must be paid to this issue? Can one make the crude approximation of using smoothing for the center frequency of a pulse?

In pulsed experiments, the early arrivals form branches which correspond to wave energy propagating at the larger angles near θ_{max} . Depending on the range of propagation, the late arrival portion of the signal may be constrained to a narrower range of propagation angles. Is more smoothing appropriate for this portion due to the θ_{max} factor in λ_{min} ?

The measure $C_{\Delta V}$ is quite generally a function of range. Yet, we mainly used 1000 km propagation in our calculations to determine the optimal amount of smoothing and neglected the range dependence; we did note however a weak range dependence. Recall that several approximations are made arriving at the parabolic equation or other one-way, small-angle approximation variants. The neglected terms may also put range dependence in the propagation, and it would not make sense to try to be more accurate with the smoothing than the level of these other approximations. A more detailed understanding of the effects of neglected terms would be desirable.

Although, there is significantly less micro-folding for the smoothed than for the unsmoothed potentials, there is still uncertainty as to how much improvement is gained for the optimal smoothing. This could be made clear by carrying out the full detailed semiclassical construction and comparing it to the wave field propagation; we will carry this out in Ref. 19. A much deeper understanding would come from a full theory based on applying the area- $(\lambda_0/2\pi)$ rule discussed in Sec. IV C. It would give the most precise answers possible to questions of which structures are physically irrelevant and which method removes them in the most optimal way. We are pursuing this investigation because only by separating out the physically irrelevant fine structures can we begin to fully address the ray chaos conundrum and know whether it can be overcome.

ACKNOWLEDGMENTS

We gratefully acknowledge M. G. Brown for a critical reading of the manuscript and for the support of the Office of Naval Research through the grant N00014-98-1-0079 and the National Science Foundation through the grant PHY-0098027.

APPENDIX A: THE SPLIT-OPERATOR, FAST FOURIER TRANSFORM METHOD

The parabolic equation in Eq. (4) describes the propagation of an acoustic wave with Hamiltonian $H = p^2/2 + V$, where $p^2/2$ and V denote the kinetic and potential energies. A wave field can be advanced exactly through the application of the unitary

propagation operator $\exp(-ik_0 \int H dr)$. The split-operator Fourier transform method²² approximates this operator using $e^{A+B} \approx e^{A/2} e^B e^{A/2}$, where A is taken to be $-ik_0 \int (p^2/2) dr = -(i/k_0) \int (k^2/2) dr$ and B is taken to be $-ik_0 \int V(z, r) dr$. Inserting a Fourier transform identity and rearranging terms before integrating gives a formula for the propagation of a wave field, $\Psi_\omega(z, r)$, at a range r to a wave field, $\Psi_\omega(z, r')$, at a range $r' = r + \Delta r$

$$\Psi_\omega(z, r') = F^{-1} \left[e^{A/2} F \left[e^B F^{-1} \left[e^{A/2} F [\Psi_\omega(z, r)] \right] \right] \right] \quad (\text{A1})$$

where F and F^{-1} are the forward and backward Fourier transforms, respectively. This equation has error $O\left((k_0 \Delta r)^3\right)$ due to the operator approximation. We approximate the integral $\int_r^{r'} V(z, r) dr \approx \Delta r [V(z, r) + V(z, r')]/2$ and perform the integration $\int_r^{r'} (k^2/4) dr = \Delta r k^2/4$.

The wave fields in this paper are calculated over a vertical grid of $z \in [-2, 7]$ km. The reflection boundary condition at the surface is not enforced in favor of the wave experiencing a soft reflection from the potential rather than a hard reflection from the surface. Wave energy which is reflected from the surface is eventually absorbed by the bottom in long range propagations so that this energy is negligible at a receiver. The soft reflections of the wave are due only to the background portion of the potential (Munk's canonical model in Eq. (8)) whose effects have been extended above the surface, $z < 0$. The internal wave fluctuations from Eq. (9) are cut off by the surface filter in Eq. (10) so that they don't have an effect on the wave above the surface.

The grid size for the propagation is chosen to be dependent on the source frequency (to ensure proper sampling of the source in the horizontal and vertical directions) and the maximum number of vertical modes, J (to ensure proper sampling of the smallest wavelengths in each vertical mode). The grid number in the depth direction is purposely chosen to be a power of 2 to allow the use of a fast Fourier transform for the split-operator Fourier method. Specifically, for the source frequencies 25, 75, 150, 250 Hz, we chose $\Delta r = 0.01, 0.01, 0.005, 0.0025$ km and $\Delta z = 9/N$ km where $N = 1024, 2048, 2048, 2048$, respectively. These values are large enough to guarantee proper convergence of the split-operator method for the propagation.

APPENDIX B: IMPLEMENTATION OF INTERNAL WAVE SOUND SPEED MODEL

The efficient numerical scheme devised by Colosi and Brown¹⁷ generates a random ensemble of internal wave effects for the sound speed model, $\delta c_{iw}(z, r)/c_0$, through the following equation:

$$\frac{\delta c_{iw}(z, r)}{c_0} = \frac{24.5}{g} \frac{2B}{\pi} N_0^2 \sqrt{\frac{E \Delta k_r}{M}} \exp(-3z/2B) \quad (\text{B1})$$

$$\times \sum_{j=1}^{J_{max}} \sum_{k_r=k_{min}}^{k_{max}} \sin(j\pi\xi(z)) \sqrt{\frac{I_{j,k_r}}{j^2 + j_*^2}} \cos(\phi_{j,k_r} + k_r r)$$

where

$$k_j I_{j,k_r} = \frac{1}{\beta^2 + 1} + \frac{1}{2} \frac{\beta^2}{(\beta^2 + 1)^{\frac{3}{2}}} \ln \left(\frac{\sqrt{\beta^2 + 1} + 1}{\sqrt{\beta^2 + 1} - 1} \right) \quad (\text{B2})$$

A single random seed generates the random phases, $\phi_{j,k_r} \in [0, 2\pi)$, for each internal wave with vertical mode, j , and horizontal wavenumber, k_r . These random phases give the ocean a different internal wave realization for each random seed. All calculations in this paper were done with a single realization of the internal wave field, but all results are similar for averages over ensemble of internal wave fields as well. Each internal wave in the superposition has the statistics of the Garrett-Munk spectrum. The full Garrett-Munk energy of $E = 6.3 \times 10^{-5}$ has been used in all calculations. Our calculations are done for a latitude of 30° so that the inertial frequency is $f_i = 1$ cycle per day. The buoyancy profile is assumed to have the form $N(z) = N_0 e^{-z/B}$, where $N_0 = 1$ cycle per 10 min is the buoyancy frequency at the surface. We considered the depth of the ocean to be $H = 5.0$ km, even though we extended the propagation range to the region $[-2, 7]$ km for the reasons described in Appendix A.

The particular functional forms and constants used in this paper are as used by Colosi and Brown. Some of these forms and constants have already been identified in the body of the paper (i.e. near Eq. (9)), while the others are listed here. We took the gravitational acceleration $g = 9.81$ m/s², $M = (\pi j_* - 1)/2j_*^2$ and the principle mode number $j_* = 3$. We took 512 horizontal internal wave numbers equally spaced by Δk_r for $k_r \in 2\pi[0.01, 1.0]$ cycles per km. In the expression for I_{j,k_r} , we took $k_j = f_i \pi j / N_0 B$ and the ratio $\beta = k_r / k_j$.

Acoustic Tomography (Cambridge U. P., Cambridge, 1995).

- ² Y. V. Lvov and E. G. Tabak, "Hamiltonian formalism and the Garrett-Munk spectrum of internal waves in the ocean," *Phys. Rev. Lett.* **87**, 168501 (2001), nlin.CD/0105007.
- ³ P. F. Worcester, B. D. Cornuelle, M. A. Dzieciuch, W. H. Munk, B. M. Howe, J. A. Mercer, R. C. Spindel, J. A. Colosi, K. Metzger, T. G. Birdsall and A. B. Baggeroer, "A test of basic-scale acoustic thermometry using a large-aperture vertical array at 3250-km range in the eastern North Pacific Ocean," *J. Acoust. Soc. Am.* **105**, 3185-3201 (1999).
- ⁴ J. A. Colosi, E. K. Scheer, S. M. Flatté, B. D. Cornuelle, M. A. Dzieciuch, W. H. Munk, P. F. Worcester, B. M. Howe, J. A. Mercer, R. C. Spindel, K. Metzger, T. G. Birdsall and A. B. Baggeroer, "Comparisons of measured and predicted acoustic fluctuations for a 3250-km propagation experiment in the eastern North Pacific Ocean," *J. Acoust. Soc. Am.* **105**, 3202-3218 (1999).
- ⁵ B. D. Dushaw, G. Bold, C. -S. Chui, J. A. Colosi, B. D. Cornuelle, Y. Desaubies, M. A. Dzieciuch, A. Forbes, F. Gaillard, J. Gould, B. M. Howe, M. Lawrence, J. Lynch, D. Menemenlis, J. Mercer, P. Mikhaelovsky, W. H. Munk, I. Nakano, F. Schott, U. Send, R. Spindel, T. Terre, P. F. Worcester, and C. Wunsch, "Observing the ocean in the 2000's: A strategy for the role of acoustic tomography in ocean climate observation," in *Observing the Oceans in the 21st Century*, edited by C. J. Koblenz and N. R. Smith (GODAE Project Office and Bureau of Meteorology, Melbourne), 391-418, (2001).
- ⁶ J. B. Keller, "A Geometrical Theory of Diffraction," in *Calculus of Variations and its Applications, Proceedings of Symposia in Applied Mathematics*, edited by L. M. Graves, Volume 8, 27-51 (McGraw-Hill, New York, 1958).
- ⁷ J. B. Keller, "Geometrical Theory of Diffraction," *J. Opt. Soc. Am.* **52**, 116-130 (1962).
- ⁸ D. R. Palmer, M. G. Brown, F. D. Tappert, and H. F. Bezdek, "Classical chaos in nonseparable wave propagation problems," *Geophys. Res. Lett.* **15**, 569-572 (1988).
- ⁹ M. V. Berry, N. L. Balazs, M. Tabor and A. Voros, "Quantum Maps," *Ann. Physics* **122**, 26-63 (1979).
- ¹⁰ M. V. Berry and N. L. Balazs "Evolution of semiclassical quantum states in phase space," *J. Phys. A* **12**, 625-642 (1979).
- ¹¹ G. M. Zaslavsky, "Stochasticity in Quantum Systems," *Phys. Rep.* **80**, 157-250 (1981).
- ¹² G. P. Berman and G. M. Zaslavsky, "Condition of stochasticity of quantum nonlinear systems," *Physica A* **91**, 450-460 (1978).
- ¹³ M. A. Sepulveda, S. Tomovic, and E. J. Heller, "Semi-classical propagation: How long can it last?," *Phys. Rev. Lett.* **69**, 402-405 (1992).
- ¹⁴ S. Tomovic, and E. J. Heller, "Long-time semiclassical dynamics of chaos: The stadium billiard," *Phys.*

¹ W. H. Munk, P. F. Worcester and C. Wunsch, *Ocean*

- Rev. E **47**, 282-299 (1993).
- ¹⁵ F. D. Tappert, "The Parabolic Approximation Method," in *Wave Propagation and Underwater Acoustics*, edited by J. B. Keller and J. S. Papadakis, Topics in Current Physics, Volume 8 (Springer-Verlag, Berlin, 1977).
 - ¹⁶ W. H. Munk, "Sound Channel in an exponentially stratified ocean with applications to SOFAR," *J. Acoust. Soc. Am.* **55**, 220-226 (1974).
 - ¹⁷ J. A. Colosi, and M. G. Brown, "Efficient numerical simulation of stochastic internal-wave induced sound-speed perturbation fields," *J. Acoust. Soc. Am.* **103**, 2232-2235 (1998).
 - ¹⁸ W. H. Munk and C. Garrett, "Internal waves in the ocean," *Annu. Rev. Fluid Mech.* **11**, 339-369 (1979).
 - ¹⁹ K. C. Hegewisch, N. R. Cerruti and S. Tomsovic, preprint.
 - ²⁰ J. Simmen, S. M. Flatté and G.-Yu Wang, "Wavefront folding, chaos and diffraction for sound propagation through ocean internal waves," *J. Acoust. Soc. Am.* **102**, 239-255 (1997).
 - ²¹ R. H. Hardin and F. D. Tappert, "Application of the split-step Fourier method to the numerical solution of nonlinear and variable coefficient wave equations," *SIAM Rev.* **15**, 423 (1973).
 - ²² J. A. Fleck and M. D. Feit, "Time-Dependent Propagation of High Energy Laser Beams through the Atmosphere," *Appl. Phys.* **10**, 129-160 (1976).
 - ²³ S. M. Flatté, R. Dashen, W. H. Munk, K. M. Watson, and F. Zachariasen, *Sound Transmission through a Fluctuating Ocean* (Cambridge U.P., Cambridge, 1979).
 - ²⁴ B. M. Howe, J. A. Mercer, R. C. Spindel, P. F. Worcester, J. A. Hildebrand, W. S. Hodgkiss, Jr., T. Duda, and S. M. Flatté, "Slice89: A single-slice tomography experiment," In J. Potter and A. Warn-Varnas, editors, *Ocean Variability and Acoustic Propagation*, 81-86. Kluwer Academic Publishers, 1991.
 - ²⁵ T. F. Duda, S. M. Flatté, J. A. Colosi, B. D. Cornuelle, J. A. Hildebrand, W. S. Hodgkiss, Jr., P. F. Worcester, B. M. Howe, J. A. Mercer, and R.C. Spindel, "Measured wave-front fluctuations in 1000-km pulse propagation in the Pacific Ocean," *J. Acoust. Soc. Am.* **92**, 939-955 (1992).
 - ²⁶ M. G. Brown and J. Viechnicki, "Stochastic ray theory for long-range sound propagation in deep ocean environments," *J. Acoust. Soc. Am.* **104**, 2090-2104 (1998).
 - ²⁷ D. Huber, E. J. Heller and R. G. Littlejohn, "Generalized Gaussian wave packet dynamics, Schrödinger equation, and stationary phase approximation," *J. Chem. Phys.* **89**, 2003-2014 (1988).
 - ²⁸ M. G. Brown, J. A. Colosi, S. Tomsovic, A. L. Virovlyansky, M. A. Wolfson, and G. M. Zaslavsky, "Ray dynamics in long-range deep ocean sound propagation," *J. Acoust. Soc. Am.* **113**, 2533-2547 (2003), nlin.CD/0301026.
 - ²⁹ L. B. Schulman, "Techniques and Applications of Path Integration," (John Wiley and Sons, 1981).
 - ³⁰ E. J. Heller, "Wavepacket Dynamics and Quantum Chaology" in *Chaos and Quantum Physics*, edited by M.-J. Giannoni, A. Voros, and J. Zinn-Justin, Les Houches Session LII 1989 (Elsevier, Amsterdam, 1991).
 - ³¹ P. Grassberger, R. Badii and A. Politi, "Scaling laws for invariant measures on hyperbolic and non-hyperbolic attractors," *J. Stat. Phys.* **51**, 135-178 (1988).
 - ³² M. A. Wolfson and S. Tomsovic, "On the stability of long-range sound propagation through a structured ocean," *J. Acoust. Soc. Am.* **109**, 2693-2703 (2001), nlin.CD/0002030.
 - ³³ F. J. Beron-Vera and M. G. Brown, "Ray stability in weakly range-dependent sound channels," *J. Acoust. Soc. Am.* **114**, 123-130 (2003), nlin.CD/0208038.
 - ³⁴ P. F. Worcester, B. M. Howe, J. A. Mercer, M. A. Dzieciuch, and the Alternate Source Test (AST) Group (T. G. Birdsall, B. M. Howe, J. A. Mercer, K. Metzger, R. C. Spindel, and P. F. Worcester), "A comparison of long-range acoustic propagation at ultra-low (28 Hz) and very-low (84 Hz) frequencies," in *Proc. of the US-Russia Workshop on Experimental Underwater Acoustics*, edited by V.I. Talanov, Nizhny Novgorod: Institute of Applied Physics, Russian Academy of Sciences, 93-104 (2000).